Journal of Materials Chemistry A

ROYAL SOCIETY OF CHEMISTRY

PAPER

View Article Online
View Journal | View Issue

Cite this: J. Mater. Chem. A, 2022, 10, 6231

Photocatalytic degradation of methylene blue (MB) with Cu_1–ZnO single atom catalysts on graphene-coated flexible substrates†

Ping Rong,‡[a] Ya-Fei Jiang, ‡[b] Qi Wang,[c] Meng Gu,[c] Xue-Lian Jiang[b] and Qi Yu *[a]

Defects can predominantly dictate the properties of oxide materials, in particular, photocatalytic and electrical properties. By implanting the defects of metallic element, Cu atom doped ZnO (Cu_1–ZnO) supported by graphene-coated polyethylene-terephthalate (GPET) transparent substrate has been successfully synthesized *via* hydrothermal method. Our Cu–ZnO/GPET presents a high enhancement of photocatalytic activity by ultraviolet (UV) light illumination, with the degradation efficiency of methylene blue (MB) as high as 83.6%, which is superior to pure ZnO/GPET photocatalyst. Cu can be observed in the form of single atoms through HAADF-STEM tomography. First-principles theoretical calculations show that the d-states of Cu atoms in Cu_1–ZnO/GPET become closer to the Fermi level than those of Zn atoms. Upon UV irradiation, doped Cu metal atoms could capture electrons in the conductive band of Cu_1–ZnO/GPET and help to separate photogenerated electrons and holes *via* monovalent Cu and O atoms. Then, electron-rich Cu atoms could activate O_2 to form superoxide radicals while the generated holes as oxygen-centered radicals could react with water to form highly active hydroxyl radicals, thus effectively degrading the MB solution.

Received 21st November 2021
Accepted 7th January 2022

DOI: 10.1039/d1ta09954j

rsc.li/materials-a

1. Introduction

Single atom catalysis has become a popular frontier in the field of heterogeneous catalysis since this concept was first proposed in 2011.[1,2] The high atomic utilization efficiency of metal atoms and precisely designed active sites contribute to the high catalytic performance of single atom catalysts (SACs).[3,4] Single metal atoms anchored on supports such as oxides, bulk metals, and two dimensional carbon materials have been successfully applied in thermo-catalysis and electrocatalysis,[5] but relatively few in photocatalysis.[6] The reported photocatalysis of SACs mainly focuses on hydrogen evolution, CO_2 reduction, and a few other types of reactions.[7] Because of the outstanding light absorption, ultrastability, and capability for anchoring noble metal centers, graphitic carbon nitride (g-C_3N_4) has been used to construct SACs and exhibits good photocatalytic activity towards CO_2 reduction.[8] Similarly, single metal atoms (such as Mn) embedded in nitrogen-doped graphene have also been synthesized and show high activity for water oxidation.[9] Besides, a series of nano-metal oxides such as ZnO, TiO_2, Al_2O_3, MoO_3, and binary-metal oxides (*e.g.*, $BiWO_4$, $SnWO_4$, $CoWO_4$) have also been investigated in photocatalytic applications.[10]

Among the reported photocatalysts, zinc oxide (ZnO), as a common n-type semiconducting material with proper bandgap and non-toxic character, has been applied in many photocatalytic reactions, especially for pollutant degradation. Based on the redox capacity of the photocatalyst under ultraviolet or visible light irradiation, semiconductor oxides are found to environmentally degrade non-biodegradable organic dyes and purify polluted water.[11,12] Doping metal ions into the lattice of semiconducting oxides is usually an efficient way to enhance photocatalytic performance.[13] Photogenerated electrons can be successfully transferred to doped metal atoms, which can assist charge separation in the semiconductor, as well as supply active electrons for the reduction of adsorbates. Hsieh and Ting[14] reported the Cu-doped ZnO/graphene material, which could change the energy bandgap of ZnO and improve the degradation efficiency of methyl orange. Yousefi and coworkers[15] reported that incorporation of Mg into ZnO nanoparticles could induce the Fermi level to move to the conductive band and enhance the electron transfer rate of the catalyst to dye pollution, thereby improving the photocatalytic activity of ZnO nanostructures under visible light. Doping other metals such as Fe^{3+} and Al^{3+} into ZnO nanostructures were also studied to improve their photocatalytic activity.[16,17]

[a]School of Materials Science and Engineering, Shaanxi Laboratory of Catalysis, Shaanxi University of Technology, Hanzhong 723001, China. E-mail: kukukoko2004@163.com

[b]Department of Chemistry, Southern University of Science and Technology, Shenzhen 518055, China

[c]Department of Materials Science and Engineering, Southern University of Science and Technology, Shenzhen 518055, China

† Electronic supplementary information (ESI) available. See DOI: 10.1039/d1ta09954j

‡ These authors contributed equally

Integrating the semiconducting material with two-dimensional carbon materials can improve the energy efficiency of photocatalysts.[18,19] Among various hybrid nanostructures, the popular graphene with zero bandgap, large surface area, high carrier mobility, conductivity, and transparency is ideal in reducing the bandgap in the semiconductor and restraining recombination efficiency of electron–hole, thus improving its photocatalytic performance.[20,21] For example, Xu *et al.*[21] have fabricated ZnO/graphene materials with porous network structures through chemical etching technique, exhibiting the degradation rate of methyl orange up to 87% in 3 h under visible light. Also, Thangavel *et al.*[22] prepared the ZnO/graphdiyne nanohybrid by hydrothermal method with superior photocatalytic activity, which exhibited degradation rates of 68% for methylene blue (MB) degradation under ultraviolet irradiation. However, most of the reported ZnO photocatalysts supported by 2D carbon materials prepared have powder morphology, which hampers their wide practical applications due to the difficulty of solid–liquid separation and recovery. Thus, developing thin film photocatalysts is necessary and imperative for industry applications.

On the other hand, MB as a cationic phenothiazine dye for biological colorant, leather industries, as well as for printing and textiles, has been found to be difficult to degrade utterly. However, MB has severe adverse effects on the biological systems of humans and animals. Therefore, the chemical degradation of MB is a critical contaminating model system for photocatalytic design. Here, we have successfully synthesized Cu single atom doped ZnO nanofilms supported by transparent graphene-coated polyethylene-terephthalate substrates (GPET) *via* a one-step growth method. Photocatalytic degradation of MB by this new SAC is then evaluated. Combined with first-principles theoretical calculations, we unveil the photodegradation mechanism of Cu-doped ZnO/GPET catalyst and the significant role of doped Cu atoms in promoting photocatalytic activity. The theoretical results can provide insights for understanding SAC-based photocatalysis in general.

2. Experimental

2.1. Synthesis of Cu–ZnO nanocluster on GPET substrate

The Cu–ZnO nanoclusters (NCs) were successfully synthesized on the GPET substrate. ZnO buffer layers (~30 nm thickness) were first coated on the GPET substrate by the sputtering method. As precursor solutions, zinc nitrate and hexamethylenetetramine need to be blended in 30 mL distilled water. Copper nitrate was added for the dopant with a concentration of 0.1 mol L^{-1}. The solution was stirred for 30 min. After that, the liquid was loaded into an autoclave at 95 °C for 6 h. Finally, the products were washed and dried naturally.

2.2. Structural characteristics

The field-emission scanning-electron microscope (FE-SEM) was utilized to observe the composite microscopic morphology, and the X-ray diffraction (XRD) was used for determining the crystal texture. X-ray photoelectron spectroscopy (XPS) was adopted to analyze surface elements and chemical states of the samples. High-resolution high-angle annular dark field technique of scanning transmission electron microscopy (HAADF-STEM) was used to analyze Cu atoms dispersed on the ZnO substrate. The photoluminescence (PL) spectra (wavelength 325 nm) were also taken to analyze the optical properties. Theoretical calculations with density functional theory (DFT) were performed to provide insights into the electronic structures of Cu_1/ZnO and the photocatalytic process.

2.3. Photocatalytic measurement

The photocatalytic properties were investigated through degrading MB dye under UV irradiation. 50 mL MB solution was put into the reactivator. The substrates were rinsed under a spot of MB that was soaked in the reactor under dark conditions. The reagents needed to be churned for 30 min to achieve adsorption and desorption equilibria. After that, the samples were kept under a 500 W Xe-lamp for the analysis of photocatalytic performance. The samples were taken every 30 min, and the absorbance of the MB solution was measured by a UV spectrophotometer.

2.4. Theoretical calculations

First-principles DFT calculations have been carried out by using Vienna *ab initio* Simulation Package (VASP 5.4.4).[23] The spin-polarized Kohn–Sham formalism was adopted using generalized gradient approximation (GGA) with the exchange-correlation functional of Perdew–Burke–Ernzerhof (PBE).[24] The projector augmented wave method (PAW)[25] was used to account for the core-valence interaction. Planewave basis functions were used with a cutoff energy of 520 eV in reciprocal space. A gamma centered Monkhorst–Pack $18 \times 18 \times 9$ grid was used to sample the Brillouin zone for bulk calculations while gamma points only for supercell slab calculations. Atomic positions were optimized until the forces were below 0.02 eV $Å^{-1}$, and the energy convergence was required to reduce to below 10^{-5} eV. To correct for the strong local correlation of Zn and Cu 3d states and O 2p states for better band gap, DFT+U method[26,27] was used with Hubbard-*U* values of 10.5 eV for Zn 3d electrons, 4.5 eV for Cu 3d electrons, and 7.0 eV for O 2p electrons.[28–30]

Based on the most stable wurtzite ZnO cells, an oxygen-terminated ZnO (002)-p(3×3) surface slab was taken to represent the periodic slab model. The slab consists of twelve atom layers, where the bottom six atom layers were frozen while the other layers were relaxed during the energy minimization. The Cu_1@ZnO doped model was constructed by replacing one surface Zn atom with one Cu atom, and Cu_1/ZnO supported model was built by binding one Cu atom on the surface oxygen atoms. The supercell slabs were repeated periodically with a 15 Å vacuum layer between the images in the surface normal direction to avoid artificial interactions.

The formation Gibbs free energy of doped Cu_1@ZnO and supported Cu_1/ZnO are defined as,

$$\Delta G(Cu_1@ZnO) = G(Cu_1@ZnO) - G(Cu^{2+}(aq)) - G(ZnO) + G(Zn^{2+}(aq))$$

$$\Delta G(Cu_1/ZnO) = G(Cu_1/ZnO) - G(Cu^{2+}(aq)) - E(ZnO)$$

where the Gibbs free energy of $Zn^{2+}(aq)$ and $Cu^{2+}(aq)$ were calculated through equation $M(g) \rightarrow M^{2+}(aq) + 2e^-$. That is,

$$G(M^{2+}(aq)) = E(M(g)) + \Delta G(0\ K \rightarrow 298.15\ K) + \Delta_f G^\circ(M^{2+}(aq)) - \Delta_f G^\circ(M(g)).$$

Here $\Delta_f G^\circ$ is the standard Gibbs energy of formation for Zn(g), Cu(g), $Cu^{2+}(aq)$, and $Zn^{2+}(aq)$.[31] The other computational details are given in the ESI†.

3. Results and discussion

3.1. Morphology and structure of Cu–ZnO/GPET composites

FE-SEM imaging technique is performed to observe the micro-morphology of samples (Fig. 1a and b). Undoped ZnO has a vertically arranged nanorod (NRs) structure, implying that ZnO/GPET has a coincident orientation. Meanwhile, the size of the NCs is enlarged with Cu atoms added, in which the irregular NRs are joined together, as observed in Fig. 1b. It manifests that Cu doping can influence the growth mechanism of ZnO. The XRD peak positions of the nanomaterials are largely keeping with the standard card (ZnO JCPDS no. 36-1451), indicating that Cu-doped nanomaterial maintains hexagonal wurtzite structure as that of standard ZnO (Fig. 1c). No appearance of impurity

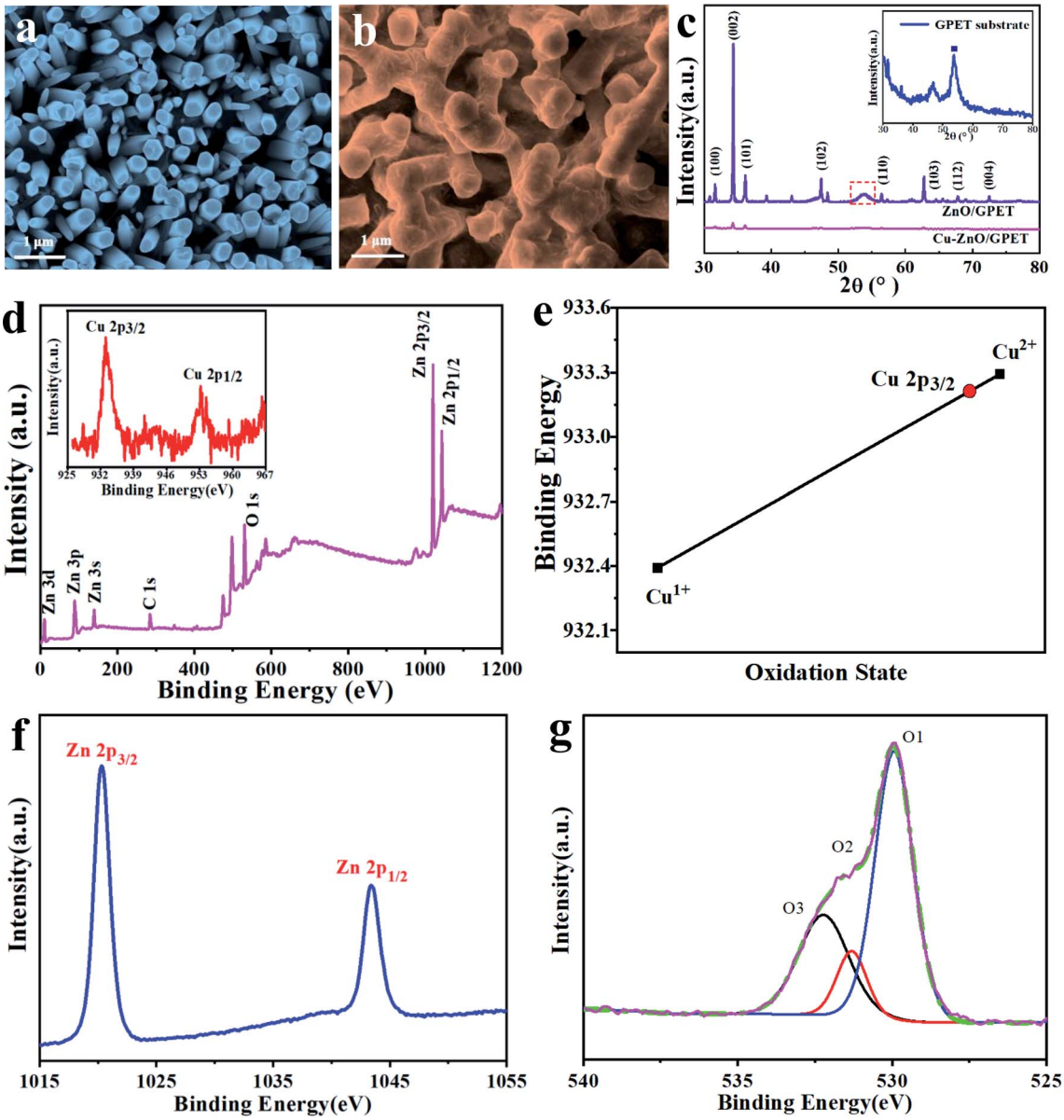

Fig. 1 The FESEM images of (a) ZnO/GPET and (b) Cu_1–ZnO/GPET. (c) The XRD patterns of ZnO/GPET and Cu_1–ZnO/GPET nanomaterials, where inset shows GPET substrate peaks. (d) XPS spectra for Cu_1–ZnO/GPET films and the inset shows Cu 2p peaks. (e) The binding energy of Cu $2p_{3/2}$ with +2 and +1 oxidation states, respectively. (f and g) High resolution XPS scan of Zn 2p and O 1s for Cu_1–ZnO/GPET.

peak after Cu doping proves that Cu has doped in ZnO lattice as ions. In the synthesized wurtzite crystals, the intensity of the (002) diffraction peak is visibly higher than others, meaning that it has an obvious *c*-axis preferential orientation. The peak intensities of ZnO/GPET doped with Cu are weaker than that of the pure sample, implying that Cu doping will influence the crystallinity of ZnO.

To analyze the surface elements and oxidation states of ZnO/GPET nanofilms doped with Cu metal, the XPS spectrum is presented in Fig. 1d. There are 3 forms of strong electron detachment peaks in accordance with Zn, O, and C elements. The C 1s exhibits a single peak at 284.6 eV that belongs to sp^2 hybrid carbon atoms.[32] The inset is the XPS of Cu 2p that reveals two distinct peaks of Cu $2p_{3/2}$ and Cu $2p_{1/2}$ at 933.2 eV and 953.4 eV, consistent with the literature.[33] As shown in Fig. 1e, the $2p_{3/2}$ binding energy of Cu is close to that of the Cu(II) oxidation state, as reported before.[34,35] These binding energies are also consistent with the statistically averaged ones of Cu^{1+} (932.4 eV) and Cu^{2+} (933.3 eV) from the NIST XPS database (Fig. 1e).[34–36] Therefore, one can deduce that Cu exists as ionic Cu(II) single atoms on ZnO, unlike that in bulk copper.[35] The binding energies at around 1020.3 eV and 1043.4 eV correspond to $2p_{3/2}$ and $2p_{1/2}$ levels of Zn^{2+} ions (Fig. 1f).[37,38] Meanwhile, the distance between the two main peaks is 23 eV, which is identical with the ZnO energy splitting.[37,38] O 1s XPS peaks for Cu_1–ZnO/GPET are composed of three typical XPS peaks (marked as O1, O2, and O3, respectively), as shown in Fig. 1g. The peak O1 at low binding energy is ascribed to the Zn–O bond, while the peak O2 is attributed to O^{2-} ions at the oxygen deficient area of ZnO. The peak at higher binding energy (O3) is usually correlated to the existence of adsorbed or loosely bound oxygen species on the sample surface (for example, CO_3, absorbed H_2O, and O_2),[39] further confirming the substitution of Zn^{2+} with the Cu ion.

To further confirm the single-atom status of Cu, we carried out the HAADF scanning transmission electron microscope (STEM) and the energy dispersive X-ray spectroscopy (EDS) analysis. In Fig. 2a, the detailed morphology and composition were studied by transmission electron microscopy, showing excellent uniform dispersion. Fig. 2b shows the uniform distribution of C, Zn, Cu, and O elements in Cu_1–ZnO determined by EDS analysis in STEM. From the line intensity distribution diagram of Cu atoms (Fig. 2c), the intensity near the center is significantly reduced. These HAADF-STEM images (Fig. 2d) clearly show that Cu atoms are spatially isolated and dispersed on the ZnO substrate (as observed in the red contrast point), and they have replaced surface Zn atoms on some specific sites. These HAADF-STEM results and XPS data provide solid credence of Cu existing as single atoms in Cu–ZnO/GPET.

3.2. Photoluminescence and photocatalytic performance

The prepared ZnO nanofilms were radiatively excited under 325 nm light at room temperature to obtain the PL properties.

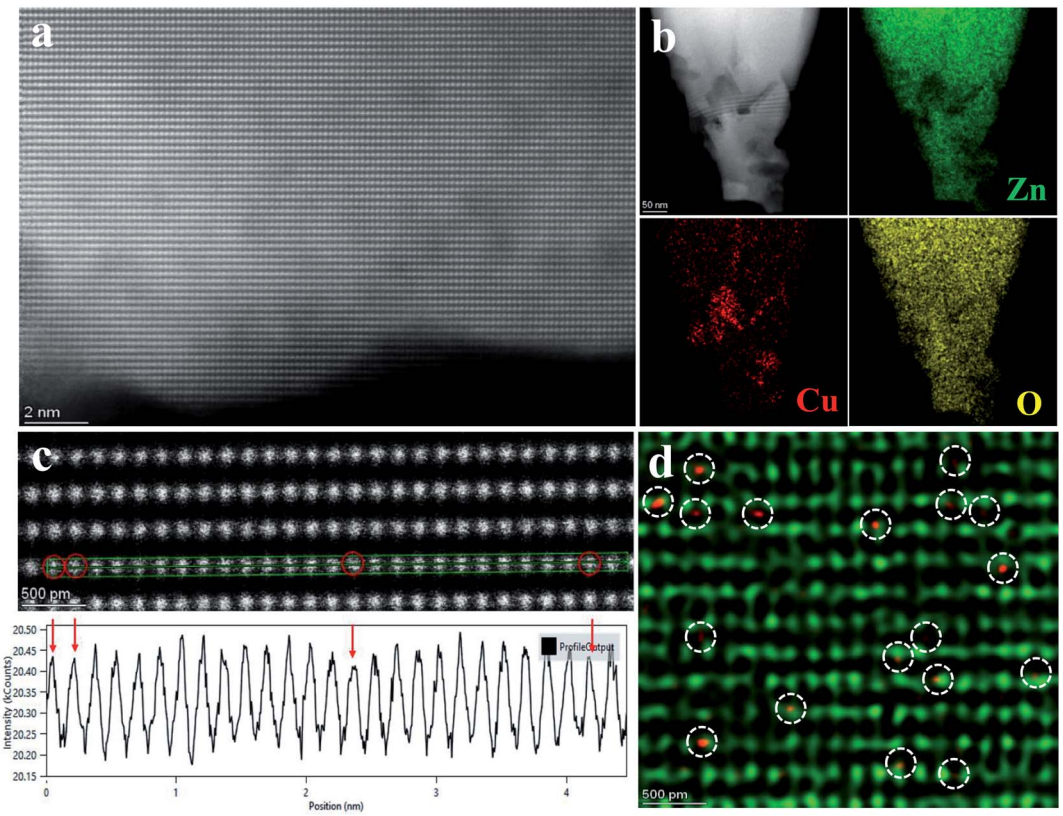

Fig. 2 (a) TEM images for Cu–ZnO. (b) STEM-EDS elemental mapping of Cu–ZnO. (c) Line intensity distribution diagram of Cu atoms. (d) HAADF STEM image of Cu_1–ZnO. The representative Cu single atom (Cu_1) is indicated by the white circle.

Fig. 3a shows the PL spectrum of pure ZnO/GPET and Cu_1–ZnO/GPET films. Both films have strong UV emission peaks near 389 nm, which is generally considered to arise from the radiative recombination of photogenerated electrons and holes.[40,41] However, Cu_1–ZnO/GPET has a much lower emission intensity than pure ZnO/GPET, implying that the efficiency of electron–hole pair recombination on Cu_1–ZnO/GPET is dramatically reduced. Thus, these doped metal ions could capture electrons, and the doping of Cu metal elements in pure ZnO/GPET could effectively suppress the recombination of photogenerated carriers. Lower photoluminescence intensity of photocatalysts usually means lower efficiency of recombination of photogenerated charges (e^-, h^+) and higher photocatalytic performance.[42] Therefore, the photocatalytic activity of ZnO/GPET is intensified by doping Cu single atoms on the surface.

In order to shed light on the mechanism of photocatalysis, the MB^+ geometric structure has been optimized using the PBE/6-31G method with the Gaussian program and is shown in Fig. 3b. To assess the photocatalytic performance of the Cu_1–ZnO/GPET composite, we investigate the MB degradation by UV light (320 nm < λ < 400 nm).[43,44] Fig. 3c exhibits the change of UV-visible absorption spectrum with MB solution for Cu_1–ZnO/GPET photocatalyst by UV light irradiation. Because the absorbance of MB solution is directly proportional to its concentration, we can easily get its concentration variation with light irradiation time. The MB degrades gradually with the increase in photocatalytic time. After 7 h UV irradiation, the photo-induced MB decomposition was only 45.6% without photocatalysts, while it approaches 69.1% under pure ZnO/GPET photocatalysts (Fig. 3d), indicating that pure photolysis of MB has rather low efficiency. As expected from the superior electron–hole separation, doping Cu metal atoms into ZnO/GPET photocatalysts increases the degradation rate of MB significantly to 83.6%. Thus, we conclude that Cu-doping as single atoms on the ZnO surface promotes the photocatalytic activity of ZnO/GPET.

3.3. Theoretical studies and mechanism analysis

In order to understand the electronic structures and photocatalytic performance, we performed periodic DFT calculations. Since graphene is used mainly to facilitate conductivity, it has not been considered in the model calculations. Our calculations show that doped Cu_1@ZnO is thermodynamically more stable than the two types of supported Cu_1/ZnO and will be the dominant structure in the Cu–ZnO/GPET system (Fig. 4). Based on the optimized most stable doped and supported structures shown in Fig. 4b and c, the projected density of state (pDOS) of Cu_1@ZnO and Cu_1/ZnO are calculated as shown in Fig. 5a and b. We find that pDOS of Cu atom d-states are located closer to

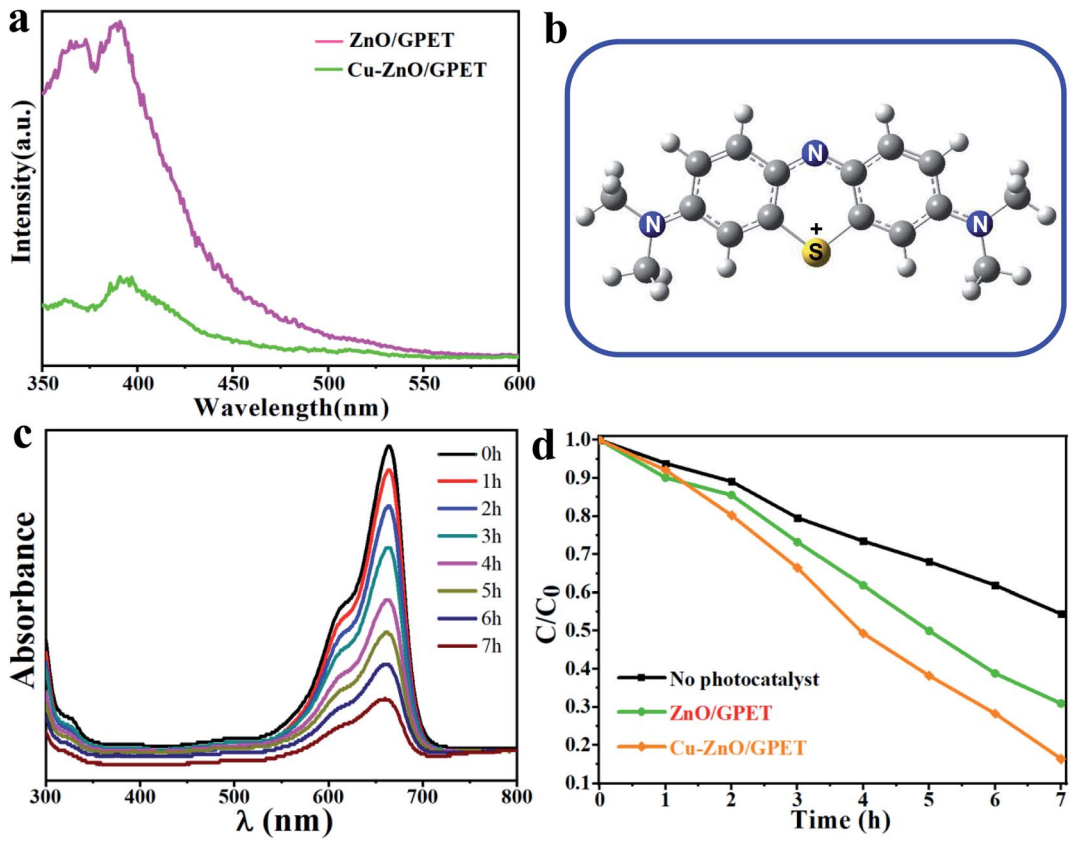

Fig. 3 (a) PL spectra of the Cu_1–ZnO/GPET composite. (b) Schematic structure of MB^+ cation (optimized by using PBE/6-31G with Gaussian program). (c) Temporal evolution of the UV-vis absorption spectrum in accord with MB of Cu_1–ZnO/GPET. (d) Photodegradation rate of MB stimulated by UV of samples.

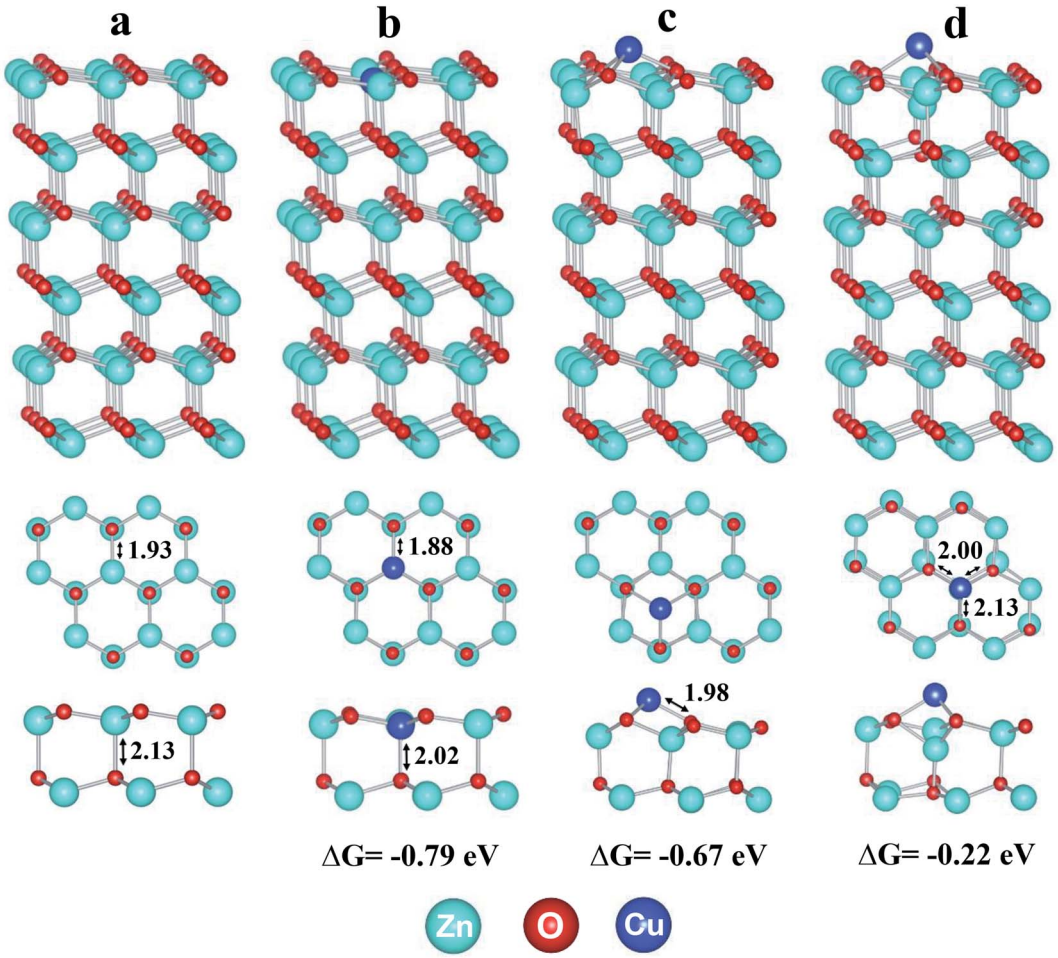

Fig. 4 The optimized structures of (a) pure ZnO, (b) doped Cu_1@ZnO, and (c and d) supported Cu_1/ZnO. The formation Gibbs free energies of doped and supported Cu_1 are calculated at 298.15 K and 1 atm. The blue, cyan, and red spheres represent Cu, Zn, and O, respectively.

the Fermi energy level than that of Zn atoms, and there are vacant Cu d-states, implying that photogenerated electrons could possibly lie at the doped Cu atoms upon light irradiation and recombination of photogenerated electrons and holes is then partially hindered. The band structures of pure and Cu-doped ZnO bulk were calculated using the DFT+U approach[26,27,45] to obtain an improved band gap and electronic structure information of Cu_1–ZnO/GPET. The band gap for pure ZnO is calculated as 2.08 eV (Fig. 5c), and it is reduced to 1.63 eV after Cu doping, with the Cu band coming across the Fermi level (Fig. 5d), implying unoccupied 3d states on Cu atoms. This result further confirms the previously proposed role of doped Cu and enhanced photocatalytic mechanism.

With the results of the electronic and band structure information of the Cu_1@ZnO model system, we will turn to the structure of MB and explore the probable photocatalytic mechanism. The Mulliken net charges calculated with the PBE/6-31G method of the Gaussian program show that the S atom exhibits a positive charge of +0.59 $|e^-|$, while the net charges of bridging N and terminal N atoms are -0.48 $|e^-|$ and -0.58 $|e^-|$, respectively, implying that the cationic S representation of the MB^+ structure (Fig. 3b) is appropriate. In general, the MB species features cyclic reduction and oxidization properties, in which MB can either convert into the colorless and reduced leuco MB or the colored oxidized form upon exposure to reducing or oxidizing agents, respectively.[46,47] Particularly, as one of the best photo-sensitizers, MB can generate singlet oxygen upon exposure to light or undergo various oxidation reactions by interacting with oxidizing radicals arising from photogenerated electrons and holes of the photocatalyst under light irradiation. In the current SAC photocatalyst, MB^+ cation can easily be attacked by various O-containing radicals in the solution near the Cu_1 site, where the activated O_2^- species or other O-containing radical species can directly react with S atom and $-CH_x$ group to trigger the photodegradation.

Based on the calculated band structure and pDOS shown in Fig. 5, following the general notion, one can largely infer that with UV light irradiation, the electrons are excited from the valence band (VB) maximum to the conductive band (CB) minimum and positively charged holes (h^+) will be generated in the VB, thus forming electron–hole pairs. Therefore, curbing the radiative and non-radiative electron–hole recombination holds the key to having good performance for photocatalysts. Since the HAADF-STEM and XPS data have shown that Cu(II)

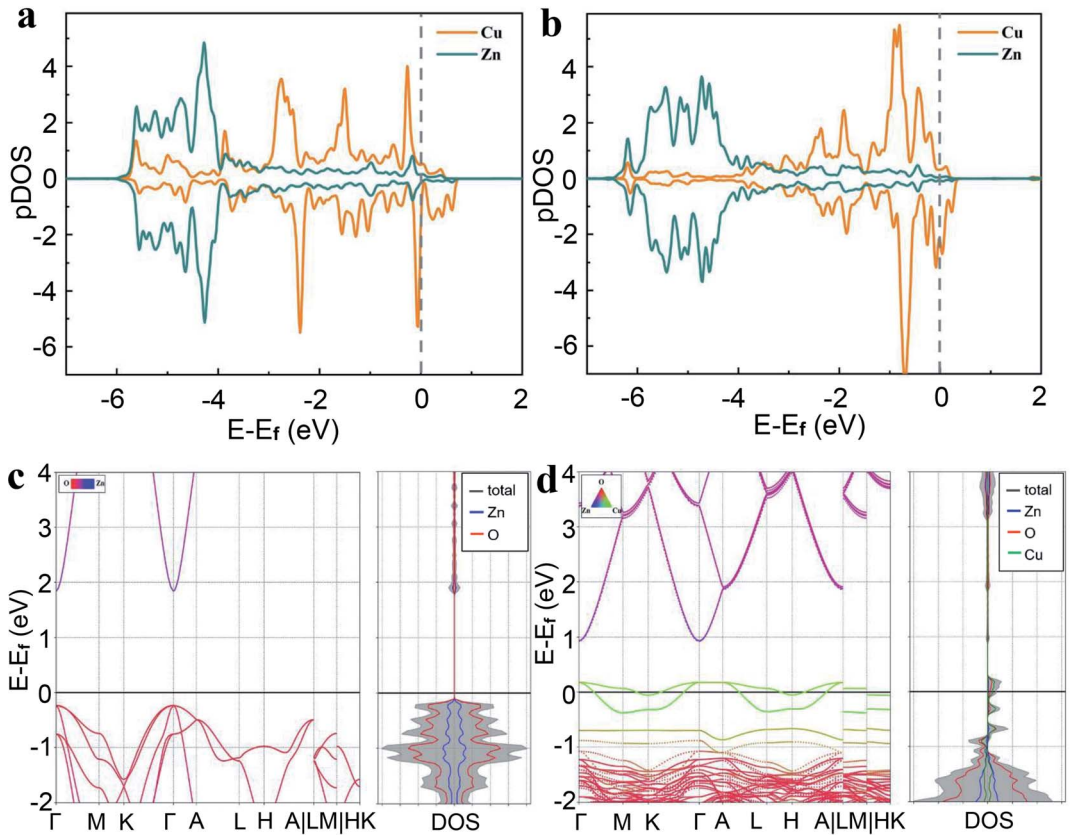

Fig. 5 Projected density of state (pDOS) of surface Zn and Cu atoms in (a) doped Cu_1@ZnO model (Fig. 4b), and (b) supported Cu_1/ZnO model (Fig. 4c). Band structure of (c) pure ZnO and (d) doped Cu_1@ZnO in which one Zn atom in the 2 × 2 × 2 supercell of ZnO is replaced by one Cu atom.

atoms replace the Zn(II) atoms, as shown in Fig. 6a, the optimized structure confirms that the Cu_1 atom has a local C_{3v} symmetry and is four-fold coordinated by three quasi-equatorial O atoms at 1.88 Å and one axial O atom at 2.02 Å, with the ∠OCuO bond angles of 116.6° (equatorial) and 100.6° (axial), respectively. These Cu–O distances are markedly shorter than those in the un-doped ZnO, with three Zn–O at 1.93 Å and one Zn–O at 2.13 Å while the ∠OZnO bond angles lie at 117.3° (equatorial) and 99.6° (axial), respectively. In the local C_{3v} ligand field of four oxygen atoms with axial Cu–O along the C_3 axis, the d-states of Cu_1 single atoms will split into quantized energy levels in the order of $e(xz, yz) << e(x^2 - y^2, xy) < a_1(z^2)$. With the $3d^9$ configuration of Cu_1, there will be a hole on its $3d_{z^2}$ orbital, which will play a vital role in the photocatalysis of Cu_1@ZnO where Cu(II, d^9) is converted in aqueous solution into less stable Cu(I, d^{10}) upon UV irradiation (Fig. 6c).

As the d-states of Cu_1 single atoms lie at the conductive band minimum, with the ligand–metal charge transfer (LMCT) transition, the electrons will transit from O 2p band to Cu $3d_{z^2}$ orbital-based vacant states under UV or even visible light, which is in direct contrast with the scenario in un-doped ZnO, where under UV-light, the electrons will transit from O 2p band to highly diffuse Zn 4s/4p vacant states because Zn 3d-bands are fully occupied (although 4s-band of Zn will also be partially occupied when Zn(II) is reduced to Zn(I) at the oxygen-defect sites). We have calculated the charge density difference (CDD) and Bader charges, as shown in Fig. S1 of the ESI file.† The Bader charges are +1.176 |e| for Zn, −1.177 |e| for O, and +1.193 |e| for Cu, respectively, indicating Cu is slightly more positively charged than Zn when replacing the latter on the ZnO surface. The calculated CDDs (Fig. S1†) and Bader charge analysis of Cu_1/ZnO active site reveal charge depletion at the Cu atoms and charge accumulation at the equatorial and axial O atoms. Upon light radiation with appropriate energy ($h\nu$), the non-bonding 2p lone-pair electron on the surface O-atom will be excited to the Cu 3d empty orbitals through ligand–metal charge transfer (LMCT). This LMCT upon UV-radiation causes the electron–hole separation, which then respectively leads to reduction of O_2 by electrons (e^-) and oxidization of H_2O (or organics) by holes (h^+). The transition probabilities are also evaluated following the dipole–velocity approximation *via* the momentum operator.[48,49] The calculated band structures and corresponding transition probabilities for the majority spin of undoped ZnO and doped Cu_1@ZnO using PBE functional are shown in Fig. S3 of the ESI file.† It turns out that the doped Cu_1@ZnO not only has a much smaller band gap but also much larger transition probabilities than undoped ZnO, consistent with the improved photocatalytic performance of copper doping.

The Cu 3d orbitals have slightly less contracted radial distribution probabilities than Zn 3d ones (Fig. 6b); they can

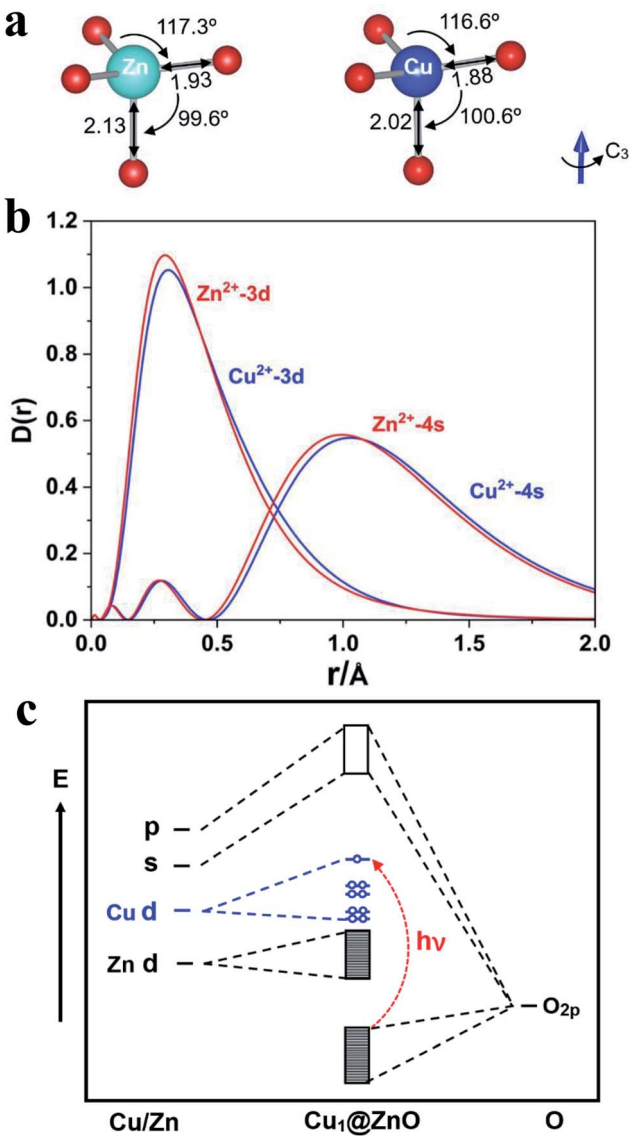

Fig. 6 (a) The local C_{3v} ligand field of ZnO and doped Cu_1@ZnO surface in crystal (color code: Cu-blue, O-red, Zn-green). (b) The radial distribution probability density ($D(r) = r^2R(r)^2$) of atomic orbitals (AOs) of Zn(II) and Cu(II); (c) schematic energy levels of the Cu_1@ZnO single-atom catalyst.

therefore bind with the O atoms of ZnO stronger than Zn atoms do, as revealed by the optimized distances and bond angles (Fig. 6a). This higher binding ability of Cu atoms may contribute to better stability of the catalyst during photocatalysis. Especially noteworthy is the well-known fact that Cu 3d orbitals are much more contracted than the Zn 4s/4p orbitals, with the orbital radii (r_{max}) of radial density maximum at ~1/4 Å for Cu 3d and ~1 Å for Zn 4s/4p, respectively. As a result, the photogenerated electrons at Cu 3d-states are much harder to recombine with O 2p-holes when compared with recombination of photogenerated electrons at Zn 4s/4p states because the electron (Cu 3d)–hole (O 2p) orbital overlap and transition dipole moment will be much smaller than those of Zn 4s/4p and O 2p. In other words, doping of Cu atoms into ZnO can impede the recombination of photogenerated electrons and O 2p holes. This result can be explained by the well-known Fermi's golden rule,[50] which states that a transition will proceed slower if the coupling between the initial and final states becomes weaker. The radiative recombination rate is related to the transition dipole moment, $\mu_{eh} = \langle \Psi_h | \hat{\mu} | \Psi_e \rangle$, where $\hat{\mu}$ is the electric dipole operator, Ψ_h and Ψ_e are the hole and electron wavefunctions, respectively.[48]

The photogenerated electron at the Cu(I) site can easily reduce triplet $^{\cdot\cdot}O_2$ into highly oxidizing doublet $^{\cdot}O_2^-$ or hydroperoxyl ($^{\cdot}$OOH) radical (R-1, R-2), which can lead to the formation of H_2O_2 or eventually $^{\cdot}$OH radicals in the aqueous solution, where there exists H_2O <=> $H^+ + OH^-$ equilibrium (R-3–R-5). The adsorption geometries and energies of O_2, OH, and OOH on the Cu_1@ZnO single atom catalyst are calculated, and the results are shown in Table S1 (ESI†). The Gibbs free energies of the two reaction paths are also calculated, as shown in Table S2 and Fig. S2 of the ESI file.† These results are consistent with our explanation of the reaction mechanism, especially the $^{\cdot}$OOH conversion to HOOH (R-3) is much more favorable than dehydration into atomic O atoms.

$$Cu^{1+}(d^{10}) + {}^{\cdot\cdot}O_2 \rightarrow Cu^{2+}(d^9) + {}^{\cdot}O_2^- \quad \text{(R-1)}$$

$$Cu^{2+}(d^9) + {}^{\cdot}O_2^- + H^+ \rightarrow Cu^{2+}(d^9) + {}^{\cdot}OOH \quad \text{(R-2)}$$

$$Cu^{1+}(d^{10}) + {}^{\cdot}OOH + H^+ \rightarrow Cu^{2+}(d^9) + HOOH \quad \text{(R-3)}$$

$$Cu^{1+}(d^{10}) + HOOH + H^+ \rightarrow Cu^{2+}(d^9) + {}^{\cdot}OH + H_2O \quad \text{(R-4)}$$

$$Cu^{1+}(d^{10}) + {}^{\cdot}O_2^- + 2H^+ \rightarrow Cu^{2+}(d^9) + 2{}^{\cdot}OH \quad \text{(R-5)}$$

Meanwhile, due to low electron–hole recombining efficiency with Cu_1@ZnO single atom catalyst, the holes (h^+) generated on the O 2p based VB can thus have enough time to react with water or directly with organic compounds bearing some functional groups (H-FG) to form active hydroxyl radicals ($^{\cdot}$OH)[51] and organic radicals ($^{\cdot}$FG) (R-6 and R-7). The highly active $^{\cdot}$OH radicals generated at the Cu and O sites can both react with MB dye solvated in the solution as strong oxidizing agents.

$$h^+ + H_2O \rightarrow {}^{\cdot}OH + H^+ \quad \text{(R-6)}$$

$$h^+ + \text{H-FG} \rightarrow {}^{\cdot}FG + H^+ \quad \text{(R-7)}$$

The specific mechanism of MB photocatalytic degradation is unquestionably complicated and involves numerous reaction channels with multi-steps. A detailed investigation of all the elementary reaction steps involved in MB photodegradation is beyond the scope of this work. Following the literature discussion and our results, the proposed reaction scheme is outlined in Fig. 7. In general, the oxidation reactions of MB include the generation of various intermediates and final products. Overall, the degradation experiences the following processes successively, photogenerated electrons and holes to facilitate the formation of $^{\cdot}$OOH, $^{\cdot}$OH, H^+, and other organic radicals ($^{\cdot}$FG). The –S, –N, and $–CH_x$ groups are subject to attack by the highly oxidizing O-containing radical species or protons, leading to sulfur/nitrogen-oxidation, demethylation, aromatic rings

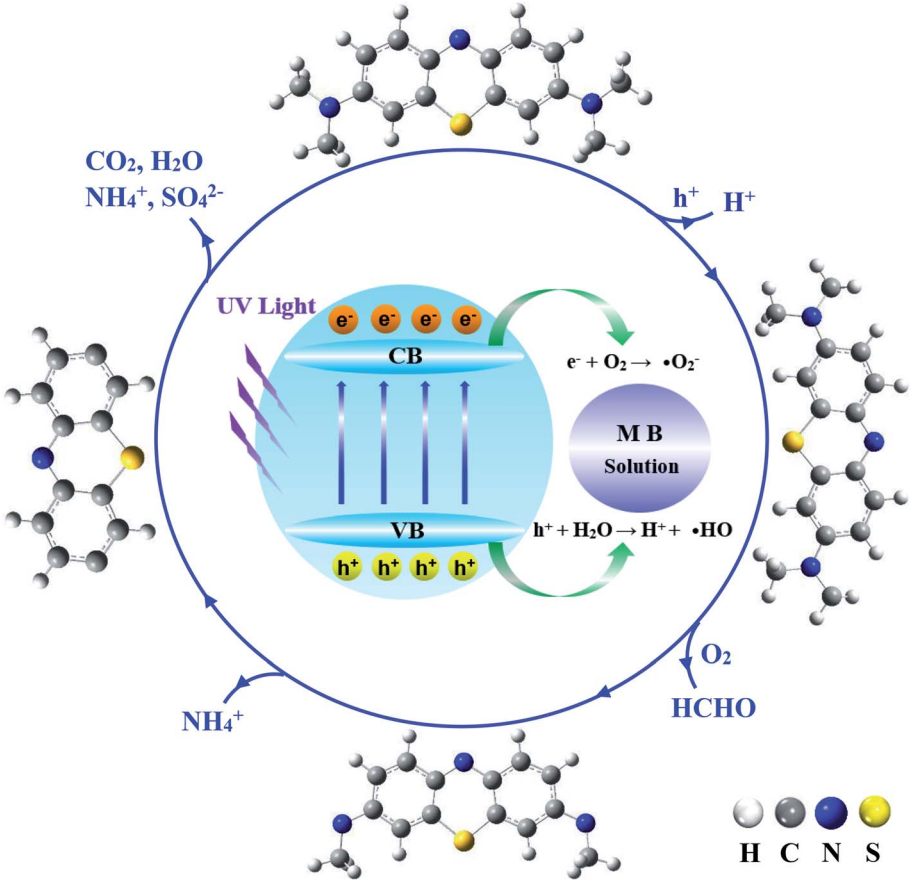

Fig. 7 Schematic illustration of the MB photodegradation mechanism of photocatalysis. Outside structures show the proposed intermediates and products of MB photocatalytic degradation.

fracture, and eventually radical fragments converting to intermediates and final products.[52,53]

As discussed earlier, the open 3d-shell of Cu(II) will play a key role for photogenerated electrons, which accelerates the formation of $^{\bullet}O_2^-$, $^{\bullet}OOH$, and $^{\bullet}OH$ radicals. Meanwhile, the O 2p based holes as oxygen-centered radicals extract electrons from water or organics to afford $^{\bullet}OH$, $^{\bullet}FG$, and proton (H^+). As has been extensively discussed in the literature, by attacking the –S, –N atoms and C–H bonds or dehydration of $–CH_x$ functional groups by $^{\bullet}OH$, MB will be eventually oxidized into various intermediate species with partially oxidized S, N, C species, leading to the formation of final products (SO_4^{2-}, CO_2, H_2O, NH_4^+, and NO_3^-).[44,54] Especially, by attacking the $–CH_x$ functional group by O-containing radicals, the terminal $–N(CH_3)_2$ group will be decomposed *via* hydrogen abstraction and oxidation, which further results in demethylation to a radical ring structure. The aromatic stability of the ring structure will be destroyed, and the rings will be eventually fragmented to allow further oxidation. Depending on the pH and other thermodynamic conditions, some triplet $^{\bullet\bullet}O_2$ molecules can easily adsorb on the surface of Cu_1@ZnO and obtain electrons to produce active superoxide radical anions ($^{\bullet}O_2^-$).[55] The ring structure can also be attacked by $^{\bullet}O_2^-$, resulting in the formation of intermediates and further reaction to the last products as mineral.[54]

4. Conclusions

In this paper, Cu–ZnO nanoclusters have been successfully prepared on flexible graphene substrates *via* a one-step method. The samples have hexagonal wurtzite structures for ZnO, even though the doping of Cu metal ions can influence the crystallinity. HAADF-STEM and XPS measurements show the successful doping of single Cu element, the surface composition of Cu–ZnO/GPET, and the chemical oxidation states of the metal elements. Especially, they provide evidence for the successful preparation of single-atom catalyst Cu_1@ZnO/GPET. Our synthesized Cu_1@ZnO/GPET material exhibits enhanced photocatalytic activity towards the degradation of methylene blue solution. We demonstrate that doping Cu single atoms change the properties of ZnO/GPET significantly. Based on the performance of the Cu_1@ZnO photocatalyst, we propose that this kind of non-noble metal catalyst featuring single-atom doped ZnO combined with suitable 2D carbon materials can play a significant role in the photocatalytic degradation of other organic pollutants as well.

Conflicts of interest

The authors declare no conflict of interest.

Acknowledgements

This work is financially supported by the National Natural Science Foundation of China (No. 92061109, 22033005), Natural Science Basic Research Program of Shaanxi (Program No. S2020-JC-WT-0001), Open Project Program of Fujian Key Laboratory of Functional Marine Sensing Materials (grant no. MJUKF-FMSM202002), Shenzhen Science and Technology Innovation Committee (RCBS20200714114919174). The support of the Guangdong Provincial Key Laboratory of Catalysis (No. 2020B121201002) is also acknowledged. The computational resources are provided by the Supercomputer Center for Computational Science and Engineering (SUSTech).

References

1 B. Qiao, A. Wang, X. Yang, L. F. Allard, Z. Jiang, Y. Cui, J. Liu, J. Li and T. Zhang, *Nat. Chem.*, 2011, **3**, 634–641.
2 X.-F. Yang, A. Wang, B. Qiao, J. Li, J. Liu and T. Zhang, *Acc. Chem. Res.*, 2013, **46**, 1740–1748.
3 A. Wang, J. Li and T. Zhang, *Nat. Rev. Chem.*, 2018, **2**, 65–81.
4 J.-C. Liu, Y. Tang, Y.-G. Wang, T. Zhang and J. Li, *Natl. Sci. Rev.*, 2018, **5**, 638–641.
5 H.-Y. Zhuo, X. Zhang, J.-X. Liang, Q. Yu, H. Xiao and J. Li, *Chem. Rev.*, 2020, **120**, 12315–12341.
6 H. Zhang, G. Liu, L. Shi and J. Ye, *Adv. Energy Mater.*, 2018, **8**, 1701343.
7 S. Wang, L. Wang and W. Huang, *J. Mater. Chem. A*, 2020, **8**, 24307–24352.
8 G. Gao, Y. Jiao, E. R. Waclawik and A. Du, *J. Am. Chem. Soc.*, 2016, **138**, 6292–6297.
9 J. Guan, Z. Duan, F. Zhang, S. D. Kelly, R. Si, M. Dupuis, Q. Huang, J. Q. Chen, C. Tang and C. Li, *Nat. Catal.*, 2018, **1**, 870–877.
10 T. Hisatomi, J. Kubota and K. Domen, *Chem. Soc. Rev.*, 2014, **43**, 7520–7535.
11 S. Chen, D. Huang, M. Cheng, L. Lei, Y. Chen, C. Zhou, R. Deng and B. Li, *J. Mater. Chem. A*, 2021, **9**, 196–233.
12 A. A. Ashkarran and B. Mohammadi, *Appl. Surf. Sci.*, 2015, **342**, 112–119.
13 A. B. Djurišić, Y. H. Leung and A. M. Ching Ng, *Mater. Horiz.*, 2014, **1**, 400–410.
14 S.-H. Hsieh and J.-M. Ting, *Appl. Surf. Sci.*, 2018, **427**, 465–475.
15 R. Yousefi, J. Beheshtian, S. M. Seyed-Talebi, H. R. Azimi and F. Jamali-Sheini, *Chem.–Asian J.*, 2018, **13**, 194–203.
16 M. M. Ba-Abbad, A. A. H. Kadhum, A. B. Mohamad, M. S. Takriff and K. Sopian, *Chemosphere*, 2013, **91**, 1604–1611.
17 F. Ajala, A. Hamrouni, A. Houas, H. Lachheb, B. Megna, L. Palmisano and F. Parrino, *Appl. Surf. Sci.*, 2018, **445**, 376–382.
18 R. Leary and A. Westwood, *Carbon*, 2011, **49**, 741–772.
19 Q. Xiang, J. Yu and M. Jaroniec, *Chem. Soc. Rev.*, 2012, **41**, 782–796.
20 C. Lai, M.-M. Wang, G.-M. Zeng, Y.-G. Liu, D.-L. Huang, C. Zhang, R.-Z. Wang, P. Xu, M. Cheng, C. Huang, H.-P. Wu and L. Qin, *Appl. Surf. Sci.*, 2016, **390**, 368–376.
21 J. Xu, Y. Cui, Y. Han, M. Hao and X. Zhang, *RSC Adv.*, 2016, **6**, 96778–96784.
22 S. Thangavel, K. Krishnamoorthy, V. Krishnaswamy, N. Raju, S. J. Kim and G. Venugopal, *J. Phys. Chem. C*, 2015, **119**, 22057–22065.
23 G. Kresse and J. Furthmüller, *Phys. Rev. B: Condens. Matter Mater. Phys.*, 1996, **54**, 11169–11186.
24 J. P. Perdew, K. Burke and M. Ernzerhof, *Phys. Rev. Lett.*, 1996, **77**, 3865–3868.
25 G. Kresse and D. Joubert, *Phys. Rev. B: Condens. Matter Mater. Phys.*, 1999, **59**, 1758–1775.
26 S. L. Dudarev, G. A. Botton, S. Y. Savrasov, C. J. Humphreys and A. P. Sutton, *Phys. Rev. B: Condens. Matter Mater. Phys.*, 1998, **57**, 1505–1509.
27 V. I. Anisimov, F. Aryasetiawan and A. I. Lichtenstein, *J. Phys.: Condens. Matter*, 1997, **9**, 767–808.
28 J. Dai, Z. Suo, Z. Li and S. Gao, *Results Phys.*, 2019, **15**, 102649.
29 Z. Wang, H. Wang, L. Wang, H. Zhao, M. A. Kamboh, L. Hao, Q. Chen, K. He and Q. Wang, *Phys. E*, 2020, **115**, 113702.
30 R. M. Sheetz, I. Ponomareva, E. Richter, A. N. Andriotis and M. Menon, *Phys. Rev. B: Condens. Matter Mater. Phys.*, 2009, **80**, 195314.
31 P. Atkins, J. de Paula and J. Keeler, *Atkins' Physical Chemistry*, Oxford University Press, Oxford, 11th edn, 2017.
32 Q. Zhang, C. Tian, A. Wu, T. Tan, L. Sun, L. Wang and H. Fu, *J. Mater. Chem.*, 2012, **22**, 11778–11784.
33 P. Jongnavakit, P. Amornpitoksuk, S. Suwanboon and N. Ndiege, *Appl. Surf. Sci.*, 2012, **258**, 8192–8198.
34 G. Schön, *Surf. Sci.*, 1973, **35**, 96–108.
35 T. Robert and G. Offergeld, *Phys. Status Solidi A*, 1972, **14**, 277–282.
36 T. Robert, M. Bartel and G. Offergeld, *Surf. Sci.*, 1972, **33**, 123–130.
37 R. Sankar Ganesh, M. Navaneethan, G. K. Mani, S. Ponnusamy, K. Tsuchiya, C. Muthamizhchelvan, S. Kawasaki and Y. Hayakawa, *J. Alloys Compd.*, 2017, **698**, 555–564.
38 V. P. Singh and C. Rath, *RSC Adv.*, 2015, **5**, 44390–44397.
39 E. De la Rosa, S. Sepúlveda-Guzman, B. Reeja-Jayan, A. Torres, P. Salas, N. Elizondo and M. J. Yacaman, *J. Phys. Chem. C*, 2007, **111**, 8489–8495.
40 M. Ahmad, E. Ahmed, Z. L. Hong, N. R. Khalid, W. Ahmed and A. Elhissi, *J. Alloys Compd.*, 2013, **577**, 717–727.
41 O. Slimi, D. Djouadi, L. Hammiche, A. Chelouche and T. Touam, *J. Porous Mater.*, 2017, **25**, 595–601.
42 H. Shen, X. Zhao, L. Duan, R. Liu, H. Wu, T. Hou, X. Jiang and H. Gao, *Appl. Surf. Sci.*, 2017, **391**, 627–634.
43 S. Rtimi, C. Pulgarin, R. Sanjines and J. Kiwi, *Appl. Catal., B*, 2015, **162**, 236–244.
44 M. Li, Z. Qiang, C. Pulgarin and J. Kiwi, *Appl. Catal., B*, 2016, **187**, 83–89.
45 Z. Ma, F. Ren, X. Ming, Y. Long and A. A. Volinsky, *Materials*, 2019, **12**, 196.
46 H.-P. Jing, C.-C. Wang, Y.-W. Zhang, P. Wang and R. Li, *RSC Adv.*, 2014, **4**, 54454–54462.

47 A. Mills and J. Wang, *J. Photochem. Photobiol., A*, 1999, **127**, 123–134.
48 J. Luo, X. Wang, S. Li, J. Liu, Y. Guo, G. Niu, L. Yao, Y. Fu, L. Gao, Q. Dong, C. Zhao, M. Leng, F. Ma, W. Liang, L. Wang, S. Jin, J. Han, L. Zhang, J. Etheridge, J. Wang, Y. Yan, E. H. Sargent and J. Tang, *Nature*, 2018, **563**, 541–545.
49 V. Wang, N. Xu, J.-C. Liu, G. Tang and W.-T. Geng, *Comput. Phys. Commun.*, 2021, **267**, 108033.
50 E. Fermi, *Rev. Mod. Phys.*, 1932, **4**, 87–132.
51 H. J. Kim, M. K. Joshi, H. R. Pant, J. H. Kim, E. Lee and C. S. Kim, *Colloids Surf., A*, 2015, **469**, 256–262.
52 T. Zhang, T. Oyama, A. Aoshima, H. Hidaka, J. Zhao and N. Serpone, *J. Photochem. Photobiol., A*, 2001, **140**, 163–172.
53 Z. Yu and S. S. C. Chuang, *J. Phys. Chem. C*, 2007, **111**, 13813–13820.
54 A. Houas, H. Lachheb, M. Ksibi, E. Elaloui, C. Guillard and J.-M. Herrmann, *Appl. Catal., B*, 2001, **31**, 145–157.
55 C. Yang, W. Dong, G. Cui, Y. Zhao, X. Shi, X. Xia, B. Tang and W. Wang, *Sci. Rep.*, 2017, **7**, 3973.